A numerical investigation on the effect of rotation on the Cone Penetration Test

Xiaotong Yang[1], Ningning Zhang[2], Rui Wang[1, *], Alejandro Martinez[3], Yuyan Chen[3], Raul Fuentes[2], Jian-Min Zhang[1]

[1] Department of Hydraulic Engineering, Tsinghua University, Beijing, China

[2] Institute of Geomechanics and Underground Technology (GUT), RWTH Aachen University, Aachen, Germany

[3] Department of Civil and Environmental Engineering, University of California Davis, Davis, CA 95616, United States

*Corresponding author at: Department of Hydraulic Engineering, Tsinghua University, Beijing, China. E-mail address: wangrui_05@mail.tsinghua.edu.cn (R. Wang)

ABSTRACT

The cone penetration test (CPT) is one of the most popular in-situ soil characterization tools. However, the test is often difficult to conduct in soils with high penetration resistance. To resolve the problem, a rotary CPT device has recently been adopted in practice by rotating the rod to increase the penetrability, particularly in deep dense sand. This study investigates the underlying mechanism of the rotation effects from a micromechanical perspective using models based on the discrete element method (DEM). With rotation, the cone penetration resistance (q_c) decreases by up to 50%, while the cone torque resistance (t_c) increases gradually. These results are also used to successfully assess existing theoretical solutions. The mechanical work required during penetration was observed to keep rising as the rotational velocity increased. Microscopic variables including particle displacement and velocity field show that rotation reduces the volume of disturbed soil during penetration and drives particles to rotate horizontally, while contact force chain and contact fabric indicate that rotation increases the number of radial and tangential contacts and the corresponding contact forces, forming a lateral stable structure around the shaft which can reduce the force transmitted to the particles below the cone, thus decreasing the vertical penetration resistance.

KEYWORDS: cone penetration test; rotation effects; discrete element method; penetration resistance; microscopic analysis

List of Notations

d_{50}	particle mean size in the chamber center
D_{cc}	chamber diameter
d_c	cone diameter (mm)
H_{cc}	chamber height (mm)
ρ	particle density (kg/m^3)
N_p	number of particles
R_d	chamber/cone ratio (D_c/d_c)
n_p	cone/particle ratio (d_c/d_{50})
β	apex angle of cone tip (°)
G	shear modulus
v	Poisson's ratio
μ	friction coefficient
S_q	particle surface roughness
n_1, n_2	coefficients
v	penetration velocity
w	rotary speed
I	inertial number
$\dot{\gamma}$	shear strain rate
P	confining pressure
L_p	width of plastic zone
q_c	tip resistance in conventional CPT
t_c	torque on the cone per effective area
F_s	vertical frictional force on the shaft
T_s	torque on the shaft
A^v_{cone}	cone area projected on the vertical plane
A^h_{cone}	cone area projected on the horizontal plane

h	penetration depth
f_s	vertical frictional resistance on the shaft per penetration area
t_s	torque on the shaft per penetration area
SR	ratio of the rotation linear velocity to the penetration velocity ($\omega*d_c/2/v$)
W_{qc}	work done by vertical force on the cone
W_{tc}	work done by torque on the cone
W_{fs}	work done by vertical frictional force on the shaft
W_{ts}	work done by torque on the shaft
W_{tot}	total work required in the rotary penetration
σ	normal stress on the cone
τ	tangential stress on the cone
δ_{qc}	influence factor of rotation on the penetration resistance
δ_{tc}	influence factor of rotation on the torque resistance
q_c^{rot}	tip resistance in rotary CPT
σ	normal stress on the cone in conventional CPT
σ^{rot}	normal stress on the cone in rotary CPT
CF_{mean}	average contact force
F	deviatoric contact normal fabric tensor
$\Delta\theta$	angle interval in polar coordinates
f_n, f_t	normal and tangential components of a contact force
f_z, f_c, f_r	decompositions of a contact force
r	radius in the polar system
θ	polar angle
b	average value of polar radius
θ_0	preferential orientation
α	anisotropy strength of contact fabrics

1 Introduction

In-situ soil testing can help determine soil properties and characteristics at engineering construction sites. Appropriate soil testing is essential to help ensure project safety, stability, and success. The cone penetration test (CPT) has become a major in-situ testing tool benefiting from its quick, reliable, and continuous soil profiling (Uzielli, 2022; White, 2022). CPT soundings are performed by pushing a probe with a conical tip into the ground with a constant rate of 0.02 m/s to measure cone tip resistance q_c, sleeve friction f_s, and pore water pressure u_2. These measurements can be used in a wide range of engineering applications, such as soil classification (Robertson, 1990; Robertson et al., 1986), footing design (Lee & Salgado, 1999; Uzielli & Mayne, 2011) and pile design (Al-Baghdadi et al., 2017; API., 2011; Lehane et al., 2020; Lehane et al., 2022).

Apart from the advantages of CPT in soil profiling, the test also has several key limitations. One of the most crucial aspects is, due to insufficient pushing force and high resistance in deep and dense soils, continuous penetration is typically difficult to achieve for some applications, such as offshore wind energy piles (Zhang et al., 2019), thermal energy piles (Sani et al., 2019), and large underground structures (Wang et al., 2022; Li et al., 2023), making the penetration process slow and costly. To mitigate this limitation, attempts have been made to reduce or bypass reaction force for in-situ testing probes (White, 2022). For example, adding a lubrication system to inject water or drilling mud around the rods can reduce reaction force (Jefferies & Funegard, 1983; Yetginer-Tjelta et al., 2022), while utilizing the sleeve friction to overcome the cone tip resistance can bypass the required reaction force, which is generally used in bio-inspired burrowing robots (Chen et al., 2021; Tao et al., 2020). All these methods have shown promise in extending CPT capabilities for penetrating to greater depths with low demand for reaction force.

CPT tests accompanied by rotational motion have also received attention recently. A rotary CPT, which imposes an additional rotation motion to the conventional CPT while the tip resistance, rotation torque, and pore pressure are measured, has been introduced in the Chinese Code for In-situ Testing of Railway Engineering Geology (NRA, 2018). It offers several advantages compared to conventional CPT. Namely, (a) it can significantly improve CPT penetrability in hard soils, as rotation has been shown to reduce penetration resistance (Del Dottore et al., 2018; Tang & Tao, 2022); (b) it provides a possibility to reflect soil shear strength from the torque measurement, extending reliable CPT estimations of soil properties; (c) it can be considered as a miniature rotary press-in or screw pile and thus could offer improved design solutions for these pile types that are attracting increased attention in piling community (Cerfontaine, et al., 2023; Cerfontaine et al., 2022; Davidson et al., 2022; Ishihara et al., 2015; Sharif et al., 2021).

Several studies have been carried out to investigate the effects of rotation on penetration tests from the aspects of theoretical derivation, macroscopic and microscale analysis. Based on the hypothesis that the rotation altered the orientation of the vector of frictional resistance resulting in a reduction of the total penetration resistance, Bengough et al. (1997) developed a theoretical model to include the effect of rotation period and penetration rate on the estimation of penetration resistance. This work assumed that the soil is homogeneous and the normal stress on the cone surface is not affected by rotation. Song et al. (2011) used similar theoretical solutions to explain the reduction of tip resistance, by additionally considering the reduction of cone normal stress caused by rotation, which was confirmed by Tang and Tao (2022) based on Discrete Element Modeling (DEM) simulations. Sharif et al. (2021) investigated the effects of installation pitch (the ratio between rotational and vertical velocity) and base geometry on the installation requirements of rotary installed piles using DEM. Tang and Tao (2022) provided a micro-to-macro analysis that includes particle trajectories, vertical forces, torques, and powers involved in rotational penetration. These studies were carried out for depths of 0.25m-20m.

In this study, we simulate the rotary CPT in relatively dense sand using a DEM model to obtain macro and microscale results (Zhang et al., 2021; Zhang et al., 2019) with the aim of understanding the probe-soil interactions during rotary CPT. This study is structured as follows. First, we introduce the construction of a calibration chamber filled with a calibrated silica sand analogue and a simulation program with particular focus on the rotation effects on the probe-soil interaction. Then, macroscale results such as penetration resistance and torque are presented, followed by the comparison of these results with relevant theoretical solutions. The work required during the penetration is also analyzed. Microscopic quantities including particle displacement and velocity fields, contact force network, and contact fabric are presented to explore the interaction behavior from a particle or contact level.

2 Model description

2.1 Chamber construction

A three-dimensional (3D) virtual calibration chamber was constructed (Figure 1a) following the procedure described by Arroyo et al. (2011). The DEM simulations in this study were performed using the DEM code PFC3D (Itasca, 2017). Table 1 lists the geometrical details of the chamber. The cylindrical chamber has a diameter of 0.432 m and a height of 0.7 m. The particles filled into the specimen were scaled from the particle size distribution of Fontainebleau sand (Figure 1a) with a coefficient uniformity of 1.57. The DEM contact parameters for Fontainebleau sand (Table 2) were calibrated using a rough Hertzian contact model that implements surface roughness effects into the standard Hertzian model. For realistic material-based values, the shear modulus G was assigned as 32 GPa and the Poisson's ratio v as 0.19, which are appropriate values for SiO_2 according to industrial databases (Lucideon, 2001). The roughness S_q, which is the root mean square of the elevations of data points relative to a reference surface, was set as 0.6 μm, considered as a realistic roughness value for silica sand (Nardelli et al., 2017). The model parameters n_1 and n_2 were set as 0.05 and 5, respectively, after calibration against the results of contact experiments on Leighton Buzzard Sand (LBS) fraction A reported by Nardelli & Coop (2019) as shown in Figure 1c. More details on the calibration can be found in Zhang et al. (2021). The particle scaling method was used in previous studies to reduce the particle number and improve computational efficiency, with scaling factors of 10~50 (Arroyo et al., 2011; Cerfontaine et al., 2023; Cerfontaine et al., 2021; McDowell et al., 2012; Tang & Tao, 2021). To generate the sample with a manageable number of particles and sufficient contacts with the probe, the particle refinement method (McDowell et al., 2012) was used in this study, which upscales particle sizes with scaling factors gradually increasing from the chamber center to the outer boundary. A scaling factor of 39 was applied to the particle sizes in the central cylindrical area with a diameter of 0.086 m, making the particle median size d_{50} in the chamber center 8.19 mm while d_{50} of the real soil is 0.21mm. This scaling factor guarantees that sufficient number of particles (approximately 30) are in contact with the cone tip. The filter layers with 1.5 times scaling factor in the subsequent zones with outer diameters of 0.136, 0.198, 0.259, and 0.432 m (Figure 1a), was verified to be able to avoid the small particles migrating into larger-particle layers (McDowell et al., 2012). These gradually expanding particle layers limited the total number of particles to within 30000. The particle rotation is inhibited to roughly mimic the effect of non-spherical particle shapes (Arroyo et al., 2011; Calvetti, 2008; Ting et al., 1989). All chamber boundaries were set frictionless to mitigate boundary effects.

After the specimen was generated with sufficient uniformity, the inter-particle friction coefficient was reduced to 0.05 and an isotropic compression of 5 kPa was applied on all the chamber boundaries to attain a sample with the target initial void ratio of 0.621. The relative density of the specimen was thus determined to be 72% based on the values of maximum void ratio e_{max} and minimum void ratio e_{min} of Fontainebleau sand of 0.9 and 0.51, respectively (Ciantia, Arroyo, et al., 2019). After equilibrium, inter-particle friction was reset to the calibrated value and isotropic stress was ramped up to a target level of 200 kPa on the radial, top, and bottom walls using a servo-controlled mechanism. The application of such confining stress was to simulate soil stress at the depth of approximately 20 m. During the penetration process, only the top and radial boundaries were servo-controlled to maintain the stress level, while the bottom boundary was fixed. In all simulations, a local damping of 0.05 (Cundall, 1987) was employed and no viscous damping was considered.

The probe was composed of a cone and a shaft rod with identical diameter of 0.036 m, and the cone tip had an apex angle of 60°. Contact parameters for the probe are listed in Table 2 (Zhang et al., 2021). The cone diameter to mean particle size ratio n_p (= d_c/d_{50}) and chamber diameter to cone diameter ratio R_d (= D_c/d_c) are 4.4 and 12, respectively. Both values are higher than most of the values chosen in previous 3D DEM soil penetration studies as summarized by Chen et al. (2021).

2.2 Penetration simulations

A benchmark simulation case was a conventional CPT, in which the penetration was carried out with only a constant vertical penetration velocity and no rotation. The inertial number, *I*, can be used to characterize the dynamic effects in systems under shear:

$$I = \dot{\gamma} d_{50} \sqrt{\frac{\rho}{P}} \#(1)$$

where $\dot{\gamma}$ is the shear strain rate, d_{50} is the median diameter of the particles, ρ is the particle density and P is the confining pressure. $\dot{\gamma}$ can be calculated as $\dot{\gamma}=v/L_p$, where L_p is the width of plastic zone formed under the tip, which was assumed to be $3d_c$ following Lu et al. (2004). Ciantia et al. (2019) chose the penetration velocity v of 0.5 m/s to facilitate efficient computation while still maintaining a quasi-static status of the sample. In this study we use the same penetration velocity and the resulting I value for the benchmark simulation is 4.3×10^{-3}, smaller than the 10^{-2} threshold which is assumed for quasi-static conditions according to Janda and Ooi (2016).

A rotation velocity ω was imposed on the probe to achieve a rotary CPT case. The speed ratio (*SR)*, expressed as the ratio of the linear rotation velocity to the vertical penetration velocity $\omega d_c/(2v)$, was defined to characterize the rotary CPT motion. Note that the definition of *SR* is similar to the term of 'Installation Pitch' or 'Advancement Ratio' used for screw piles to characterize installation performance (Sharif et al., 2021). To cover an appropriate *SR* range (Sharif et al., 2021; Tang & Tao, 2021), 9 cases with different *SR* values (i.e., 0.05, 0.125, 0.5,1.0, 2.0, 3.0, 7.0, 15.0, 30.0) following a relatively uniform distribution in logarithmic scale were performed. The conventional CPT corresponds to a case with *SR* = 0.0. All simulations were conducted using an Intel i7-9700 CPU with 32GB of RAM, and the typical runtime for a rotary penetration is four to six days.

3 Macroscale results

3.1 Penetration resistance and torque

During rotary penetration, the vertical cone resistance q_c, torque on the cone per effective area t_c, vertical frictional force on the whole shaft F_s, and torque on the whole shaft T_s were recorded to characterize the soil-probe interactions. Figure 2a shows respective calculation formulas for the four quantities in conjunction with the illustration of force components acting on the shaft and cone. Figures 2b-e present the recordings of q_c, t_c, F_s, and T_s in a rotary CPT simulation with *SR* = 2.

As shown in Figures 2b and 2c, the two quantities recorded on the cone (i.e., q_c and t_c) evolve to a relatively constant value after an approximate shallow depth of 0.15 m. It should be noted that the total torque on the cone is normalized by the cone area projected on the vertical plane, i.e., A^v_{cone} = $\pi d_c l \cos(\beta/2)/2$, where l is the length of cone generatrix. The vertical force on the cone is normalized by the projected area of the cone in the horizontal plane $A^h_{cone} = \pi d_c^2/4$ to obtain the penetration resistance. The raw data present noticeable fluctuations due to the scaled-size particles. To capture the evolving features of the two quantities recorded on the cone and filter out their fluctuations, the exponential expression applied in Arroyo et al. (2011) was used in the present analyses to process the raw q_c and t_c data:

$$q_c(h)\ or\ t_c(h) = a_k \times \left(1 - e^{-b_k \times h}\right) \#(2)$$

where, h is penetration depth; a_k and b_k are fitting parameters where a_k gives the steady value of q_c or t_c at large depths and b is inversely related to the limit of shallow penetration, and subscript k refers to either q_c or t_c.

For the measurements on the shaft, the normalized penetration resistance and torque by contact area are not directly used to fit the steady values, because data fluctuation is large at the beginning of penetration due to the small contacting area. Instead, the evolution of total vertical force F_s and total torque T_s versus penetration depth are first monitored and shown in Figures 2d and 2e, which increase near linearly due to the increase of the contacting area of the shaft with the surrounding soil particles $A^v_{shaft} = \pi d_c(h\text{-}h_c)$, where h_c is the cone height. Equation (3) is used to reflect the linear increase of the total vertical friction and torque on the shaft.

$$F_s(h) or\ T_s(h) = c_t \times (h - h_c) \#(3)$$

where, c_t is a fitting parameter representing the slope of the line and subscript t refers to F_s or T_s. The fitting lines of these quantities are plotted in Figure 2. Then the steady values of vertical frictional resistance and torque on the shaft per penetration area, f_s and t_s, can be calculated as Equation (4) and (5) respectively.

$$f_s = \frac{F_s}{A^v_{shaft}} = \frac{c_{Fs} \times (h - h_c)}{\pi d_c(h - h_c)} = \frac{c_{Fs}}{\pi d_c} \#(4)$$

$$t_s = \frac{T_s}{A^v_{shaft}} = \frac{c_{Ts} \times (h - h_c)}{\pi d_c(h - h_c)} = \frac{c_{Ts}}{\pi d_c} \#(5)$$

Results of the simulated cases with varying SR are presented in Table 3. Figure 3 demonstrates the effects of rotation on the steady values of q_c and t_c as well as f_s and t_s. In the figure, SR values on the x-axis are plotted in a logarithmic scale, and each value is increased by 0.01 in order to show the conventional CPT in the logarithmic scale at SR = 0.01. The curves of t_c and t_s are S-shaped, and the curves of q_c and f_s are inverse S-shaped. Similar trends were also observed in Sharif et al. (2021). With the increase in SR, the resistance quantities q_c and f_s both decrease, the torque quantity t_s increases, while t_c increases to its peak value at SR=7 and then starts to decrease. Quantitatively, q_c is much greater than f_s, and t_c is much greater than t_s, indicating a major penetration resistance contribution from the cone. The reduction effects of rotation on the vertical resistance variables such as q_c and f_s confirm the possibility to improve CPT penetrability by imposing rotation.

3.2 Work required from the probe

Work analysis facilitates comparison of quantities extracted from the cone and shaft for the rotary CPT. In this section we extend the analysis of the rotary CPT with a focus on the rotation effects on the major energy components, based on previous studies on energy analyses in the standard penetration test (SPT) as reported by Zhang et al. (2021).

The major energy components in the simulations are: work done by vertical force on the cone W_{qc}, work done by torque on the cone W_{tc}, work done by vertical frictional force on the shaft W_{fs}, and work done by torque on the shaft W_{ts}. By summing up the four components, the total work done by the rotary penetration W_{tot} can be calculated.

W_{qc} is computed by integrating the product of the vertical force on the cone and the penetration velocity with respect of time for a given penetration depth:

$$W_{q_c} = \int_0^{t_{end}} q_c(t) A_{cone}^h v(t) dt \# (6)$$

where, t_{end} is the end time of penetration to a certain depth; $A^h{}_{cone}$ is the area of the cone projected on the horizontal plane, as illustrated in Figure 2a.

W_{tc} is computed by integrating product of the torque on the cone and the rotation velocity with respect of time for a given penetration depth:

$$W_{t_c} = \int_0^{t_{end}} t_c(h) A_{cone}^v w(t) dt \# (7)$$

where $A^v{}_{cone}$ is the area of the cone projected on a vertical plane.

W_{fs} and W_{ts} are computed in a similar way following Equations (8) and (9), respectively:

$$W_{f_s} = \int_0^{t_{end}} F_s(t) v(t) dt \# (8)$$

$$W_{ts} = \int_0^{t_{end}} T_s(t) w(t) dt \# (9)$$

Figure 4 shows the evolution of W_{qc}, W_{tc}, W_{fs}, W_{ts} and W_{tot} over the penetration depth in the case of SR = 2. All the work components and the total work increase with the depth increase. In the case of SR = 2, W_{qc} accounts for the major proportion (approximately 60%) of W_{tot} over the penetration.

The components of all input work during the penetration process to a depth of 0.6 m are listed in Table 4. Using these data, the rotation effect on the five work components can be visualized in Figure 5. With the increase of rotation, W_{tot} increases continually (Figure 5a) particularly in the cases of SR > 1.0, whereas Tang and Tao (2022) showed an optimal rotation speed with the least work required in a rotary penetration in shallow soils. The differences of soil conditions between this study and Tang and Tao (2022b) include soil depth, density, and confining pressures. Figure 5b shows the rotation effect on the proportion of each work component contributing to W_{tot}. As SR increases, both W_{qc} and W_{fs} decrease while W_{tc} and W_{ts} increase. W_{tc} is always above W_{ts} in the simulated cases, indicating that the major work input contribution of torque is from the cone. However, W_{tc} shows a slight decrease at the largest *SR* cases (when *SR*>15), while W_{ts} continues to increase with SR. Therefore, W_{ts} may eventually exceed W_{tc} at very large *SR* cases. In log scale, both the increase and decrease trends start to evolve exponentially after *SR* becomes greater than 1.0. Torque presents an increasingly dominating role in the total work input with increased rotation velocity. After *SR* becomes greater than 7.0, both work components from the torque elements (i.e., W_{tc}, and W_{ts}) exceed W_{qc}, becoming dominant parts of the work input. This is mainly due to a greater rotational displacement at larger *SR*. Unlike the exponential increase of W_{tot} with rotation, the work components present either *S*-shaped (e.g., W_{tc} and W_{ts}) or inverse *S*-shaped (e.g., W_{qc} and W_{fs}) trends.

4 Assessment of existing theoretical solutions for rotary CPT

During a conventional CPT, two stress components are generated on the cone: normal stress σ that is perpendicular to the cone surface and frictional stress τ that is parallel to the cone's generatrix (Figure 6a). Using the vertical components of σ and τ and their geometrical relationship, q_c can be calculated as:

$$q_c = \sigma(1 + \sqrt{3}\mu)\#(10)$$

Rotation of the probe alters the direction and/or magnitude of σ and τ (Figure 6b). A decrease in σ was measured in the DEM simulations as the SR was increased, as shown in Figure 7a, which also affects the τ magnitude, i.e., $\tau = \mu\sigma$. The direction of τ tilts to form an angle with the generatrix of the cone, which reduces the vertical component of τ and generates torque on the cone.

Although the rotation effect on σ is significant as demonstrated in this study, it has been neglected for simplicity in previous analytical solutions for penetration with rotation. For example, Bengough et al. (1997) assumed that σ remained unchanged with rotation in the derivation of analytical solutions for soil resistance estimation using a rotational penetration with a conical tip. Sharif et al. (2021) made the same assumption of regarding the lack of an effect of rotation in σ in developing analytical models to predict the installation torque and force for rotary-installed piles. The assumption may result in overestimation of the calculations, as proven by Tang and Tao (2022) through DEM simulations of penetration at a shallow depth.

Considering the effect of rotation on σ, Song et al. (2011) proposed analytical solutions to calculate tip resistance in rotary CPTs:

$$q_c^{rot} = \sigma^{rot}(1 + \sqrt{3}\mu\delta_{qc})\#(11)$$

where, q_c^{rot} and σ^{rot} are the tip resistance and normal stress on the cone surface, respectively, in rotary CPT; δ_{qc} is the influence factor of rotation on frictional force, as a function of penetration velocity, rotation velocity, and cone diameter (Song et al., 2011):

$$\delta_{qc} = \frac{\sqrt{3}v}{\sqrt{(\pi\omega D)^2 + \left(\frac{\sqrt{3}v}{2}\right)^2} + \frac{\sqrt{3}v}{2}}\#(12)$$

Normally, $\delta_{qc} \leq 1$, where $\delta_{qc} = 1$ only if $\omega = 0$. Equation (11) also shows that the effect of rotation on cone resistance is dependent on μ. If the cone surface is perfectly smooth (i.e., μ=0), rotation does not have an effect on cone resistance, indicating that $q_c = \sigma$ (or σ^{rot}) for both penetration scenarios with and without rotation.

Similarly, the torque resistance t_c can be derived as:

$$t_c = \frac{\sigma^{rot}\mu\delta_{tc}}{4A^v_{cone}}\#(13)$$

where A^v_{cone} is the cone surface area projected onto the vertical plane; δ_{tc} is the influence factor of rotation on torque resistance (Song et al., 2011):

$$\delta_{tc} = \frac{2}{3\pi^2\omega^3}\left[(\pi\omega D)^2 - \frac{3}{2}v^2\right]\sqrt{(\pi\omega D)^2 + \left(\frac{\sqrt{3}}{2}v\right)^2} + \frac{\sqrt{3}v^3}{2\pi^2\omega^3}\#(14)$$

where δ_{tc} approaches zero when w equals zero, while δ_{tc} approaches $2\pi D^3/3$ when w goes to positive infinity.

Figures 7b and 7c show the evolution of q_c and t_c obtained from both the DEM simulations and theoretical solutions. Note that the theoretical solutions for constant σ (Equation 10) and rotation-dependent σ^{rot} (Equation 11) values are both presented. It is clear that the DEM and theoretical results match well for both q_c and t_c by using a rotation-dependent σ^{rot}. Meanwhile, it is observed that q_c and t_c are overestimated using a constant σ because of the overestimation of the normal stress on the cone, particularly with fast rotation, which is consistent with Tang and Tao (2022).

5 Microscopic analysis

The DEM model can provide high-resolution results at the particle or contact level. In this section, microscopic observations and measurements are provided to further understand the soil-probe interaction during rotary penetration. Four representative cases following an even distribution in logarithmic scale are selected, i.e., SR = 0, 0.125, 2, and 15.

5.1 Displacement field and velocity field

Figure 8a shows the particle displacement field on a cross-section along the z-x plane that transverses along the center of the specimen when the penetration depth is 0.3 m. Each particle is represented by an arrow whose color and size indicate the displacement magnitude, while the vector shows the displacement direction. In all the selected cases, particles with the largest displacement concentrate around the shaft area. With the increase of rotation speed, the areas with clear displacement along the shaft and below the cone both shrink, the displacement magnitudes decrease, and the displacement directions tend to change from closely vertical to horizontal. Due to the projection, the *y*-component of the displacement vector (circumferential) becomes nonvisible, not showing the rotation effect. Therefore, we plot the magnitude of the *y*-component of the displacement separately. In Figure 8b, the particles projected onto the cross-section are colored based on the magnitude of their circumferential displacement. A positive value indicates displacement perpendicular to the *x*-*z* plane, pointing towards it, while a negative value indicates displacement perpendicular to the *x*-*z* plane, pointing outward from it. This indicates that the rotation of the probe causes the particles to displace circumferentially on the horizontal plane.

Figure 9 shows the velocity vectors of the particles in the same cross-section selected for the displacement fields at the depth of 0.3 m. In the case without rotation, the largest velocity vectors concentrate around and perpendicular to the cone surface, resulting from vertical penetration. The vectors along the entire shaft are oriented close to the vertical direction. With the increase of rotation, the concentration of the largest velocity vectors expands gradually from the cone area to the shaft, indicating a growing influence of rotation. Meanwhile, the velocity vectors along the shaft rotate from vertical to horizontal, which is driven by the resultant relative motion of the particles and the shaft.

5.2 Contact force chains

The visualization of the contact force network distribution in the selected rotary penetration cases can help further understand the effects of rotation from a microscale perspective. The contact force network can also offer explanations to the macroscale results presented in section 3. The lines join the centroids of contacting spheres, and their thickness is proportional to the magnitude of the normal force. Figure 10a shows 3D contact force vectors on a slice with a thickness of d_c projected on the *x*-*z* plane. In this figure, contact forces smaller than CF_{mean} are plotted in orange, and they are termed as 'weak contact forces', while contact forces greater than CF_{mean} are plotted in black and termed as 'strong contact forces', where CF_{mean} is the average contact force in each simulation. The definition of 'strong' and 'weak' contact force is consistent with Radjai et al. (1997).

It is clearly shown in Figure 10a that in all the selected cases, strong contact force chains concentrate in the areas at cone shoulder and below cone. In the two areas, strong force chains decrease with the increase of *SR*, which can be correlated to the q_c decrease with *SR*, as observed in Figure 3.The number of weak force chains increases with rotation, indicating a densifying effect caused by rotation at shaft mid-height area.

To further explore possible explanations for the macroscale results from the contact force network, we select three representative cross-sections to visualize the corresponding force chains, namely shaft mid-height, cone shoulder, and below cone, as shown in Figure 10b, 10c and 10d. Figure 10b shows that at shaft mid-height the weak contact force network densifies with rotation; Figure 10c shows that almost no weak contact forces concentrate at cone shoulder, and that contact force magnitudes change little with rotation in this region; Figure 10d shows a significant decrease in contact force magnitudes below cone, explaining the decrease of q_c with increasing *SR*.

5.3 Contact fabric analysis

Macroscopic measurements in a granular assembly are associated with microscopic variables at the contact scale, such as normal and shear contact forces and contact numbers. These variables can be comprehensively quantified and analyzed through contact fabric analyses (Oda, 1972; Wang et al., 2020; Mital et al., 2020; Wang et al., 2022), providing insights into the underlying mechanism of the rotation effects on penetration. The deviatoric contact normal fabric tensor norm ||**F**|| within the model before penetration is calculated 0.010, proving that the model is initially near isotropic. The calculation of deviatoric contact normal fabric tensor **F** is based on Satake's formulation (Satake, 1982):

$$\boldsymbol{F} = \frac{1}{N}\sum_{k=1}^{N} \boldsymbol{v^k} \otimes \boldsymbol{v^k} - \frac{1}{3}\boldsymbol{I} \quad \#(15)$$

where N is the number of contacts within the domain, $\mathbf{v^k}$ is the unit norm vector in the normal direction of the *k*th contact, **I** is the 2nd-order identity tensor.

5.3.1 Contact fabric quantification method

Three representative cylindrical zones around the probe were chosen for the contact fabric analysis, including regions of shaft mid-height, cone shoulder, and below cone (Figures 11a and 11b). To describe the 3D contact network and necessarily reflect the rotation effects in a 3D space, we establish a *z-c-r* cylindrical coordinate system in the chamber (Figure 11c), where *z, c and r* represent the vertical, the tangential, and radial directions, respectively. An inter-particle contacts force vector $\boldsymbol{f}$, composed of normal force $\boldsymbol{f_n}$ and tangential force $\boldsymbol{f_t}$, can be decomposed into three components $\boldsymbol{f_z}$, $\boldsymbol{f_c}$, and $\boldsymbol{f_r}$. Figure 11c also shows an example of an inter-particle contact projected to the *c-r, r-z,* and *c-z* planes. The most relevant projection is on the *c-z* plane because the vertical resistance and torque on the probe are calculated directly by f_c and f_z.

As an example for illustration, Figures 12a and 12b show, respectively, the angular distributions of total contact force and contact number of the projection on the *c-z* plane of the contacts at shaft mid-height, under four different rotation conditions (i.e., *SR* = 0, 0.125, 2, and 15). The angular distributions of contact fabric quantities calculated from the contacts in the selected zones can be plotted using polar histograms. The length of each bar was normalized by the maximum value in the reference CPT case with *SR*=0. Based on that, the bar length is a periodic function of the angle. Thus, the angular distributions of the quantities can be fitted using a truncated Fourier series:

$$r = b(1 + \alpha cos\,(2(\theta - \theta_0)))\#(16)$$

where, r is the radius in the polar system; θ is the polar angle; b, θ_0 and α are fitting parameters. b is the average value of polar radius, reflecting the size of the 'peanut' shaped area. θ_0 represents the preferential orientation. α represents the anisotropy. $\alpha = 0$ means that the rose diagrams present a 'circle shape' and the contact fabric is isotropic. With the increase of α, the 'circle' becomes a more elongated 'peanut', indicating a more anisotropic fabric. The fitted lines forming the 'peanut' shapes are also provided in each subplot of Figure 12. The main observations are: as *SR* increases, the shape of total contact force fabric changes from a 'peanut' shape to a 'circle' as shown in Figure 12a, indicating the transition from a highly anisotropic fabric to a more isotropic one in the *c-z* plane. A similar observation can be made for the number of contacts in Figure 12b. Additionally, the size increase of the contact number 'peanut' indicates a contact number increase with rotation at shaft mid-height (Figure 12b), quantitatively supporting the same observations from contact force chains in section 5.2.

5.3.2 Rotation effects on contact fabric

In this section we use a compacted and efficient way to exhibit the rotation effects on the contact fabric quantities b, α, and θ_0 from the fitted Equation (15) of the total contact force and contact number projection on *c-r, r-z,* and *c-z* planes for the contacts in the three representative regions. The results are organized in the order of regions below cone, cone shoulder, and shaft mid-height. For each region, the fabric metrics projected on the *c-z*, *r-z*, and *c-r* planes are analyzed sequentially.

a) Below cone

Figure 13 shows the evolution of the contact fabric in the below-cone area. In the polar coordinate system in Figure 13a, the 'circle', 'triangle', and 'star' symbols represent fabric quantities for contacts projected on the *c-z*, *r-z*, and *c-r* planes, respectively. The size of the symbols is scaled by b^3, so the bigger the symbol is in size, the greater the average value of total contact force is. The distance from a data point to the origin represents the rotating speed ratio $SR+0.01$ in log scale. The polar angle is consistent with the preferential orientation θ_0. The shades of the symbols correspond to α value, indicating the anisotropy intensity, where darker shade corresponds to stronger anisotropy.

(1) contact fabric in the *c-z* plane. For the total contact force (purple circles in Figure 13a), the symbol size (b) decreases significantly, and the preferential orientation (θ_0) tends to rotate clockwise towards *c*-direction, confirming the reduction effect of rotation on q_c. The shade of the symbols representing anisotropy remains largely unaffected by rotation. For the contact number (blue circles in Figure 13b), the symbol size (b) remains stable with rotation, while the preferential orientation (θ_0) is also constant in *z*-direction with a negligible change in anisotropy. This stability means that rotation does not disturb the contact number below cone. The evolutions of the fabric magnitude of total contact force and contact number on different projected planes are almost identical, so the discussions on the fabric magnitude,

i.e., symbol size (*b*), will not be stressed in the following two projected planes. This writing structure will also be used to describe the fabric metrics at cone shoulder and shaft mid-height.

(2) contact fabric in the *r-z* plane. For the total contact force (purple triangles in Figure 13a), the preferential orientation (θ_0) is located in an interval of 120°<θ_0<150°, deviated slightly from the normal direction of the cone surface (150°) to vertical direction (90°). This preference is determined by both the cone-pushing effect along the normal direction and the compression effect along the downward penetration direction. The dark shade of the symbols representing strong anisotropy remains unaffected by rotation. For the contact number (blue triangles in Figure 13b), its preferential orientation (θ_0) is stably located around 135° with relatively strong anisotropy.

(3) contact fabric in the *c-r* plane. For the total contact force (purple stars in Figure 13a), the preferential orientation (θ_0) tends to rotate counterclockwise slightly to the *c*-direction, which indicates that the rotation tends to enhance the tangential contact network. The shade of the symbols remains unaffected by rotation. For the contact number (blue stars in Figure 13b), the preferential orientation (θ_0) is in *r*-direction with largely unchanged anisotropy.

b) Cone shoulder

Figure 14 shows the evolution of the contact fabric at cone shoulder. The contact fabrics in this zone would be directly related to q_c and t_c. The magnitude (symbol size *b*) and anisotropy (symbol color) of the fabric metrics on the three planes show no significant change.

(1) contact fabric in the *c-z* plane, i.e., the circles in the two subplots of Figure 14. For the total contact force (purple circles in Figure 14a), the preferential orientation (θ_0) tends to rotate from *z* (90°) to *c* (<90°)-direction, indicating that the *c*-component of contact force increases and *z*-component decreases, which is consistent with the reduction of q_c and increase of t_c. For the contact number (blue circles in Figure 14b, its preferential orientation (θ_0) is largely unchanged between 20 to 60 degrees, close to the normal direction of the cone surface.

(2) contact fabric in the *r-z* plane, i.e., the triangles in the subplots of Figure 14. For the total contact force (purple triangles in Figure 14a), the preferential orientation (θ_0) is between 150° and 170°, close to the normal direction of the cone surface and tilting to the horizontal direction. Strong anisotropy due to the ongoing push of the probe to particles is visible from the dark shade of the symbols. For the contact number (blue triangles in Figure 14b), its preferential orientation (θ_0) is stably located around 175° with relatively strong anisotropy.

(3) contact fabric in *the c-r* plane, i.e., the stars in Figure 14. For the total contact force (purple stars in Figure 14a), the preferential orientation (θ_0) tends to tilt anticlockwise from dominant *r* to *c*-direction when *SR* is greater than one, indicating an increase of tangential force, which is related to t_c increase.

Significant anisotropy is shown by the dark shade of the symbols. For the contact number (blue stars in Figure 14b), the preferential orientation (θ_0) is relatively stable.

c) Shaft mid-height

Figure 15 shows the evolution of the contact fabric at shaft mid-height. Generally, more scatters in the contact fabric measurements are observed in this region.

(1) contact fabric in the *c-z* plane, i.e., the circles in Figure 15. For the total contact force (purple circles in Figure 15a), the symbol size (b) increases slightly, while the preferential orientation (θ_0) changes insignificantly with the increase of *SR*. The anisotropy of total contact force decreases with the increase of *SR*, visible from the reduced shade of the symbols. For the contact number (blue circles in Figure 15b), the symbol size (b) increases with rotation, meaning that more contacts are formed while the total contact force remains almost unchanged. The shade of the symbols remains light, indicating weak anisotropy. Due to the weak anisotropy, the orientation of total contact force exhibits strong scatter.

(2) contact fabric in the *r-z* plane, i.e., the triangles in Figure 15. For the total contact force (purple triangles in Figure 15a), the preferential orientation (θ_0) tilts clockwise to *r*-direction with increased *SR*. The total contact force becomes less anisotropic, according to the reduced shade of the symbols. For the contact number (blue triangles in Figure 15b), the preferential orientation (θ_0) tilts clockwise to *r*-direction with weak anisotropy. The contact fabrics in the *r-z* plane indicate that shaft rotation causes the particle contacts at the shaft mid-height to rotate from the vertical direction towards the horizontal *r*-direction.

(3) contact fabric in the *c-r* plane, i.e., the stars in Figure 15. For the total contact force (purple stars in Figure 15a), the preferential orientation (θ_0) tilts anticlockwise to the *c*-direction with increased *SR*, reflecting the enhancement effects of shaft rotation on tangential contacts. The total contact force becomes more anisotropic with increased *SR*, according to the darkening of the symbol shade. For the contact number (blue stars in Figure 15b), the preferential orientation (θ_0) also tilts counterclockwise to the *c*-direction dramatically.

The observation for contact fabric at shaft mid-height indicates that the contact force in this region increases significantly in the lateral direction as shaft rotation increases, corresponding to the stronger contact force chain observed in Figure 10. This means that a more stable force bearing structure is formed within the particles due to shaft rotation. Such change in contact force is in agreement with the observation of t_s increase in Figure 3, indicating rotation can reduce the probe penetration resistance, which would be beneficial for a pile installation scenario. In addition, the contact force network around the shaft would act as an anchor to transmit less force downwards, resulting in the reduced contact force and penetration resistance below the cone.

5.4 Implications and limitations

The contact fabric analysis shows how rotation changes the contact structure during the penetration process from a microscale perspective. Generally, it is obviously beneficial for both CPT and pile installation that the increased rotary speed ratio can reduce the penetration resistance. However, the tradeoff of higher speed ratio is that it requires much more torque input and energy consumption, demanding additional rig developments, more fuel use and possible CO_2 emission. For the application of rotary CPT, it is important to develop ways to inherit the abundant engineering and research experience and data of conventional CPT, and correlate the measurements from rotary CPT to those from conventional CPT, and then obtain mechanical property related soil parameters. The good agreement of monitored q_c and t_c with the theoretical results indicates the potential for calculating the soil-probe contact parameters, which is worth exploring in the future.

There are some limitations in the study that should be noted. Some of them derive from the simplified material model employed. For instance, stresses around the probe can cause particle crushing, which affects the analysis of soil-pile interface interaction and plays a fundamental role in some important geotechnical applications, e.g., pile shaft friction (Tamura et al., 2012; Yang et al., 2014). Particle crushing could be an important factor for offshore engineering applications where there is highly crushable calcareous sand. A crushable particle model such as Ciantia et al. (2015) may be employed to explore the effect of this feature.

6 Conclusions

Conventional CPT soundings can suffer from low penetrability, particularly in dense or hard soils. Rotation is investigated in this study to increase the penetrability of CPT. This study explored the rotation effects on CPT soundings using a DEM model. In total, ten CPT tests with different rotary speed ratios have been carried out while the vertical penetration velocity was maintained constant. The macroscale results such as penetration resistance, torque, and work input have been monitored and analyzed. Microscopic observations on quantities including displacement and velocity fields, contact force chains, and contact fabric provide explanations for the change of the macroscale results. The reliability of relevant theoretical derivations on penetration with rotation has also been assessed. The main findings of this work are drawn below:

- With the increase of rotation velocity, the torque resistances on the shaft t_s and on the cone t_c increase, while the vertical resistances q_c and f_s decrease.
- Although the percentage of work done by the vertical forces declines as rotating speed increases, the work done by the torque on cone and shaft increases, causing an overall increase of input work.

- In dense sand, theoretical calculation can provide acceptable prediction of penetration and torque resistances by considering the size of the cone, penetration and rotation velocity, when the change in normal stress on the cone with rotation is considered.
- Rotation reduces the volume of disturbed soil during penetration as evidenced by particle displacement and velocity fields.
- The rotation motion drives particles to rotate horizontally, especially in the region around the shaft, increasing the number of radial and tangential contacts and the corresponding contact forces, forming a lateral stable structure in this region. The lateral stable structure alongside the entire shaft can reduce the force transmitted to the particles below the cone, thus decreasing the vertical penetration resistance.

7 Acknowledgements

The financial support of the National Natural Science Foundation of China (No. 52378349), Beijing Natural Science Foundation (J210003), and the RWTH Aachen – Tsinghua Senior Research Fellowship funded by RWTH Aachen University is greatly acknowledged. This material is based upon work supported in part by the Engineering Research Center Program of the National Science Foundation under NSF Cooperative Agreement No. EEC–1449501. The fourth and fifth authors were supported by the National Science Foundation (NSF) under Award No. 1942369. Any opinions, findings, and conclusions or recommendations expressed in this material are those of the author(s) and do not necessarily reflect those of the National Science Foundation.

8 Author statements

Competing interests: The authors declare there are no competing interests.

Data generated or analyzed during this study are available from the corresponding author upon reasonable request.

9 References

Al-Baghdadi, T., Davidson, C., Brown, M. J., Knappett, J. A., Brennan, A., Augarde, C., Coombs, W., Wang, L., Richards, D., & Blake, A. (2017). CPT based design procedure for installation torque prediction for screw piles installed in sand. *8th Offshore Site Investigation and Geotechnics International Conference: 'Smarter Solutions for Future Offshore Developments,'* 346–353.

API. (2011). ANSI/API RP 2GEO: Geotechnical and Foundation Design Considerations. ISO 19901-4:2003 (Modified), Petroleum and natural gas industries-Specific requirements for offshore structures, Part 4-Geotechnical and foundation design considerations: Vol. Part 4 (1st edition). API Publishing Services.

Arroyo, M., Butlanska, J., Gens, A., Calvetti, F., & Jamiolkowski, M. (2011). Cone penetration tests in a virtual calibration chamber. *Geotechnique*, *61*(6), 525–531. https://doi.org/10.1680/geot.9.P.067

Bengough, A. G., Mullins, C. E., & Wilson, G. (1997). Estimating soil frictional resistance to metal probes and its relevance to the penetration of soil by roots. *European Journal of Soil Science*, *48*(4), 603–612. https://doi.org/10.1111/j.1365-2389.1997.tb00560.x

Calvetti, F. (2008). Discrete modelling of granular materials and geotechnical problems. *European Journal of Environmental and Civil Engineering*, *12*(7–8), 951–965.

Cerfontaine, B., Brown, M. J., Davidson, C., Sharif, Y. U., Huisman, M., & Ottolini, M. (2022). Optimised screw pile design for offshore jacket foundations in medium–dense sand. *Geotechnique Letters*, *12*(2), 114–119.

Cerfontaine, B., Brown, M. J., Knappett, J. A., Davidson, C., Sharif, Y. U., Huisman, M., Ottolini, M., & Ball, J. D. (2023). Control of screw pile installation to optimise performance for offshore energy applications. *Géotechnique*, *73*(3), 234–249.

Cerfontaine, B., Ciantia, M., Brown, M. J., & Sharif, Y. U. (2021). DEM study of particle scale and penetration rate on the installation mechanisms of screw piles in sand. *Computers and Geotechnics*, *139*. https://doi.org/10.1016/j.compgeo.2021.104380

Cerfontaine, B., Ciantia, M. O., Brown, M. J., White, D. J., & Sharif, Y. U. (2023). DEM study of particle scale effect on plain and rotary jacked pile behaviour in granular materials. *Computers and Geotechnics*, *161*. https://doi.org/10.1016/j.compgeo.2023.105559

Chen, Y., Khosravi, A., Martinez, A., & Dejong, J. (2021). Modeling the self-penetration process of a bio-inspired probe in granular soils. *Bioinspiration and Biomimetics*, *16*(4). https://doi.org/10.1088/1748-3190/abf46e

Ciantia, M. O., Arroyo, M., Calvetti, F., & Gens, A. (2015). An approach to enhance efficiency of dem modelling of soils with crushable grains. *Geotechnique*, *65*(2), 91–110. https://doi.org/10.1680/geot.13.P.218

Ciantia, M. O., Arroyo, M., O'Sullivan, C., Gens, A., & Liu, T. (2019). Grading evolution and critical state in a discrete numerical model of Fontainebleau sand. *Geotechnique*, *69*(1), 1–15. https://doi.org/10.1680/jgeot.17.P.023

Ciantia, M. O., O'Sullivan, C., & Jardine, R. J. (2019). Pile penetration in crushable soils: Insights from micromechanical modelling. *17th European Conference on Soil Mechanics and Geotechnical Engineering, ECSMGE 2019 - Proceedings*, 298–317. https://doi.org/10.32075/17ECSMGE-2019-1111

Cundall, P. A. (1987). Distinct element models of rock and soil structure. *Analytical and Computational Methods in Engineering Rock Mechanics*, 129–163.

Davidson, C., Brown, M. J., Cerfontaine, B., Al-Baghdadi, T., Knappett, J., Brennan, A., Augarde, C., Coombs, W., Wang, L., & Blake, A. (2022). Physical modelling to demonstrate the feasibility of screw piles for offshore jacket-supported wind energy structures. *Géotechnique*, *72*(2), 108–126.

Del Dottore, E., Mondini, A., Sadeghi, A., Mattoli, V., & Mazzolai, B. (2018). An efficient soil penetration strategy for explorative robots inspired by plant root circumnutation movements. *Bioinspiration and Biomimetics*, *13*(1). https://doi.org/10.1088/1748-3190/aa9998

Ishihara, Y., Haigh, S., & Bolton, M. (2015). Estimating base resistance and N value in rotary press-in. *Soils and Foundations*, *55*(4), 788–797.

Itasca, C. G. I., & Code, P. F. (2017). *Ver. 5.0*. Minneapolis.

Janda, A., & Ooi, J. Y. (2016). DEM modeling of cone penetration and unconfined compression in cohesive solids. *Powder Technology*, *293*, 60–68.

Jefferies, M. G., & Funegard, E. (1983). Cone penetration testing in the Beaufort Sea. In 1983 27–29 April 1983P220–243. Publ New York: ASCE (Ed.), *Proc Conference on Geotechnical Practice in Offshore Engineering, Austin, Texas, ASCE* (Vol. 22, Issue 5, pp. 220–243). https://doi.org/https://doi.org/10.1016/0148-9062(85)92108-4

Lee, J., & Salgado, R. (1999). Design of foundations bearing in sand based on CPT results. In *ProQuest Dissertations and Theses*. https://www.proquest.com/dissertations-theses/design-foundations-bearing-sand-based-on-cpt/docview/304532912/se-2?accountid=14426

Lehane, B. M., Liu, Z., Bittar, E. J., Nadim, F., Lacasse, S., Bozorgzadeh, N., Jardine, R., Ballard, J.-C., Carotenuto, P., & Gavin, K. (2022). CPT-based axial capacity design method for driven piles in clay. *Journal of Geotechnical and Geoenvironmental Engineering*, *148*(9), 04022069.

Lehane, B. M., Liu, Z., Bittar, E., Nadim, F., Lacasse, S., Jardine, R., Carotenuto, P., Rattley, M., & Gavin, K. (2020). A new'unified'CPT-based axial pile capacity design method for driven piles in sand. *4th International Symposium on Frontiers in Offshore Geotechnics (Postponed)*, 462–477.

Li, W.-T., Wang, R., & Zhang, J.-M. (2023). Influence of aboveground structure on connected underground structure seismic response within an integrated system. *Tunnelling and Underground Space Technology*, *134*, 105003.

Lu, Q., Randolph, M. F., Hu, Y., & Bugarski, I. C. (2004). A numerical study of cone penetration in clay. *Géotechnique*, *54*(4), 257–267.

Lucideon. (2001). *Properties: Silica - Silicon Dioxide (SiO2)*. AZoM. https://www.azom.com/properties.aspx?ArticleID=1114

McDowell, G. R., Falagush, O., & Yu, H. S. (2012). A particle refinement method for simulating DEM of cone penetration testing in granular materials. *Geotechnique Letters*, *2*(7–9), 141–147. https://doi.org/10.1680/geolett.12.00036

Mital, U., Kawamoto, R., & Andrade, J. E. (2020). Effect of fabric on shear wave velocity in granular soils. *Acta Geotechnica*, *15*(5), 1189–1203. https://doi.org/10.1007/s11440-019-00766-1

Nardelli, V., & Coop, M. R. (2019). The experimental contact behaviour of natural sands: normal and tangential loading. *Géotechnique*, *69*(8), 672–686.

Nardelli, V., Coop, M. R., Andrade, J. E., & Paccagnella, F. (2017). An experimental investigation of the micromechanics of Eglin sand. *Powder Technology*, *312*, 166–174. https://doi.org/10.1016/j.powtec.2017.02.009

National Railway Administration of the People's Republic of China. (2018). *Code for In-situ Testing of Railway Engineering Geology (TB10018-2018, J261-2018)*. China Railway Publishing House Beijing.

Oda, M. (1972). Initial fabrics and their relations to mechanical properties of granular material. *Soils and Foundations*, *12*(1), 17–36.

Radjai, F., Wolf, D. E., Roux, S., Jean, M., & Moreau, J. J. (1997). Force networks in dense granular media. *Powders & Grains 97*, 211–214.

Robertson, P. K. (1990). Soil classification using the cone penetration test. *Canadian Geotechnical Journal*, *27*(1), 151–158. https://doi.org/10.1139/t90-014

Robertson, P. K., Campanella, R. G., Gillespie, D., & Greig, J. (1986). Use of Piezometer Cone Data. *Use of in Situ Tests in Geotechnical Engineering, ASCE Specialty Conference*, 1263–1280.

Sani, A. K., Singh, R. M., Amis, T., & Cavarretta, I. (2019). A review on the performance of geothermal energy pile foundation, its design process and applications. *Renewable and Sustainable Energy Reviews*, *106*, 54–78. https://doi.org/10.1016/j.rser.2019.02.008

Satake, M. (1982). Fabric tensor in granular materials. *Proceedings of the IUTAM Symposium on Deformation and Failure of Granular Materials*, 63–68.

Sharif, Y. U., Brown, M. J., Ciantia, M. O., Cerfontaine, B., Davidson, C., Knappett, J., Meijer, G. J., & Ball, J. (2021). Using discrete element method (Dem) to create a cone penetration test (cpt)-based method to estimate the installation requirements of rotary-installed piles in sand. *Canadian Geotechnical Journal*, *58*(7), 919–935. https://doi.org/10.1139/cgj-2020-0017

Sharif, Y. U., Brown, M. J., Ciantia, M. O., Lutenegger, A. J., Pavan Kumar, P. V., Patra, S., & Haldar, S. (2021). Using discrete-element method hindcasting of screw pile performance for practical design. *Geotechnique Letters*, *11*(4), 333–339. https://doi.org/10.1680/jgele.21.00071

Song, L., Feng-Yin, L., & Li, N. (2011). On mechanism of rotary cone penetration test. *Rock and Soil Mechanics*, *32*. https://doi.org/10.16285/j.rsm.2011.s1.071

Tamura, S., Higuchi, Y., Hayashi, Y., & Yamzasaki, M. (2012). Centrifuge studies on the effects of existing piles on the end resistance and shaft friction of a new pile. *Soils and Foundations*, *52*(6), 1062–1072. https://doi.org/10.1016/j.sandf.2012.11.021

Tang, Y., & Tao, J. (2021). Effect of Rotation on Penetration: Toward a Seed Awn-Inspired Self-Burrowing Probe. In *IFCEE 2021* (pp. 149–159).

Tang, Y., & Tao, J. (2022a). Multiscale analysis of rotational penetration in shallow dry sand and implications for self-burrowing robot design. *Acta Geotechnica*, *0123456789*. https://doi.org/10.1007/s11440-022-01492-x

Tang, Y., & Tao, J. (2022b). Multiscale analysis of rotational penetration in shallow dry sand and implications for self-burrowing robot design. *Acta Geotechnica*, *17*(10), 4233–4252. https://doi.org/10.1007/S11440-022-01492-X

Tao, J. J., Huang, S., & Tang, Y. (2020). SBOR: a minimalistic soft self-burrowing-out robot inspired by razor clams. *Bioinspiration and Biomimetics*, *15*(5). https://doi.org/10.1088/1748-3190/ab8754

Ting, J. M., Corkum, B. T., Kauffman, C. R., & Greco, C. (1989). Discrete Numerical Model for Soil Mechanics. *Journal of Geotechnical Engineering*, *115*(3), 379–398. https://doi.org/10.1061/(ASCE)0733-9410(1989)115:3(379)

Uzielli, M. (2022). Non-deterministic interpretation and applications of CPT testing data. In *Cone Penetration Testing 2022* (pp. 81–93). CRC Press.

Uzielli, M., & Mayne, P. W. (2011). Serviceability limit state CPT-based design for vertically loaded shallow footings on sand. *Geomechanics and Geoengineering: An International Journal*, *6*(2), 91–107.

Wang, R., Dafalias, Y. F., Fu, P., & Zhang, J.-M. (2020). Fabric evolution and dilatancy within anisotropic critical state theory guided and validated by DEM. *International Journal of Solids and Structures*, *188*, 210–222.

Wang, R., Pinzón, G., Andò, E., & Viggiani, G. (2022). Modeling combined fabric evolution in an anisometric granular material driven by particle-scale X-ray measurements. *Journal of Engineering Mechanics*, *148*(1), 04021120.

Wang, R., Zhu, T., Yu, J.-K., & Zhang, J.-M. (2022). Influence of vertical ground motion on the seismic response of underground structures and underground-aboveground structure systems in liquefiable ground. *Tunnelling and Underground Space Technology*, *122*, 104351.

White, D. J. (2022). CPT equipment: Recent advances and future perspectives. *Cone Penetration Testing 2022*, 66–80.

Yang, Z. X., Jardine, R. J., Zhu, B. T., & Rimoy, S. (2014). Stresses Developed around Displacement Piles Penetration in Sand. *Journal of Geotechnical and Geoenvironmental Engineering*, *140*(3), 04013027. https://doi.org/10.1061/(ASCE)GT.1943-5606.0001022

Yetginer-Tjelta, T. I., Bøtker-Rasmussen, S., Rose, M., Lunne, T., Meyer, V., & Duffy, C. (2022). Development of an enhanced CPT system for Dogger Bank. *Cone Penetration Testing 2022 - Proceedings of the 5th International Symposium on Cone Penetration Testing, CPT 2022*, 267–272. https://doi.org/10.1201/9781003308829-34

Zhang, N., Arroyo, M., Ciantia, M., & Gens, A. (2021a). Energy balance analyses during Standard Penetration Tests in a virtual calibration chamber. *Computers and Geotechnics*, *133*. https://doi.org/10.1016/j.compgeo.2021.104040

Zhang, N., Arroyo, M., Ciantia, M. O., & Gens, A. (2021b). Energy balance analyses during Standard Penetration Tests in a virtual calibration chamber. *Computers and Geotechnics*, *133*. https://doi.org/10.1016/j.compgeo.2021.104040

Zhang, N., Arroyo, M., Ciantia, M. O., Gens, A., & Butlanska, J. (2019). Standard penetration testing in a virtual calibration chamber. *Computers and Geotechnics*, *111*(3), 277–289. https://doi.org/10.1016/j.compgeo.2019.03.021

Zhang, N., Ciantia, M. O., Arroyo, M., & Gens, A. (2021). A contact model for rough crushable sand. *Soils and Foundations*, *61*(3), 798–814. https://doi.org/10.1016/j.sandf.2021.03.002

Zhang, Y., Andersen, K. H., & Jeanjean, P. (2019). Cyclic p-y Curves in Clays for Offshore Structures. *Offshore Technology Conference*, 6–9. https://doi.org/10.4043/29346-MS

10 Tables

Table 1. Geometrical characteristics of DEM calibration chamber, particles, and cone.

Variable (unit)	Symbol	Value
Chamber diameter (mm)	D_{cc}	432
Cone diameter (mm)	d_c	36
Chamber height (mm)	H_{cc}	700
Particle median size in the chamber center (mm)	d_{50}	8.19
Particle density (kg/m³)	ρ	2600
Number of particles	N_p	29368
Chamber/cone ratio D_c/d_c	R_d	12
Cone/particle ratio d_c/d_{50}	n_p	4.4
Apex angle of cone tip (°)	β	60

Table 2. Calibrated contact model parameters (Zhang et al., 2021).

Element	shear modulus	Poisson's ratio	friction coefficient	roughness	model parameters	
Symbol/unit	G / GPa	v / -	μ / -	Sq /µm	n_1 / -	n_2 / -
Sand	32	0.19	0.275	0.6	0.05	5.0
Probe	200	0.2	0.275	-	-	-

Table 3. Fitting results for all the simulated tests.

Test ID	Rotation	*SR*	q_c MPa	t_c kN·m/m²	f_s kPa	t_s kN·m/m²
1(REF)	no	0.0	28.4	0.0	79.1	0.00
2	yes	0.05	28.2	1.4	83.1	0.07
3	yes	0.125	28.6	6.2	78.2	0.26
4	yes	0.5	27.5	23.6	67.7	0.61
5	yes	1	26.0	38.5	56.4	0.89
6	yes	2	23. 2	51.6	42.9	1.25
7	yes	3	21.5	56.2	35.3	1.35
8	yes	7	18.3	58.6	23.1	1.58
9	yes	15	16.2	55.2	16.0	1.75
10	yes	30	14.3	49.5	10.9	1.94

736 **Table 4.** Work input components done by the probe (unit: kJ).

Test ID	Rotation	SR	W_{tot}	W_{qc}	W_{fs}	W_{tc}	W_{ts}
1(REF)	no	0	17.9	16.6	1.54	0	0
2	yes	0.05	17.8	16.5	1.63	0.004	0.004
3	yes	0.125	18	16.5	1.54	0.167	0.104
4	yes	0.5	18.2	16.1	1.36	0.655	0.327
5	yes	1	19.2	15.2	1.14	2.14	0.944
6	yes	2	22.8	13.6	0.918	5.75	2.75
7	yes	3	26.9	12.6	0.748	9.39	4.4
8	yes	7	46	10.8	0.511	22.8	12
9	yes	15	84.3	9.55	0.36	46.3	28.3
10	yes	30	155.3	8.49	0.26	83.0	63.5

737

738

11 Figure captions

Figure 1. (a) Layout of chamber and probe, (b) particle size distribution of Fontainebleau sand, and (c) reproduction of the load-displacement curve from a single grain test.

Figure 2. (a) Schematic illustration of force calculations and soil resistances on the cone and shaft of rotary CPT with SR = 2: (b) tip resistance q_c, (c) torque on the cone t_c, (d) vertical friction force on the whole shaft F_s and (e) torque on the whole shaft T_s vs depth.

Figure 3. Rotation effects on the fitted value of tip resistance q_c, vertical friction force on the shaft f_s, torque on the cone t_c, and torque on the shaft t_s.

Figure 4. Work done at the cone and shaft during the rotary penetration for the case of SR=2.

Figure 5. Effect of rotation on (a) total work input, and (b) work components on the cone and shaft.

Figure 6. Force diagrams of (a) conventional and (b) rotary penetration test.

Figure 7. (a) Measured normal stress on the cone, (b) measured and predicted q_c (c) measured and predicted t_c versus $SR+0.01$.

Figure 8. (a) Particle displacement vectors projected on central vertical plane of a vertical section with the thickness of d_c, and (b) circumferential component of the displacement vectors in (a) when the probe penetrates to the depth of 0.3m.

Figure 9. Particle velocity field projected on central vertical plane of a vertical section with the thickness of d_c when the probe penetrates to the depth of 0.3m.

Figure 10. Contact force network of a vertical slice with the thickness of d_c (a) projected on the central vertical plane, and a horizontal slice (b) at shaft mid-height, (c) at cone shoulder, and (d) below cone projected on a horizontal plane when the probe penetrates to the depth of 0.3 m.

Figure 11. Selection of three representative zones around the probe for microscale characterizations: (a) side view and (b) plan view; (c) example of decomposition of a 3D contact vector in the *z-c-r* cylindrical coordinate space.

Figure 12. Contact fabric analysis in polar coordinates for the *c-z* projection of the contacts in the cylindrical zone of shaft mid-height: (a) total contact force and (b) contact number.

Figure 13. Contact fabric below cone projected on the *c-z*, *r-z*, and *c-r* plane: (a) total contact force and (b) contact number.

Figure 14. Contact fabric at cone shoulder projected on the *c-z*, *r-z*, and *c-r* plane: (a) total contact force and (b) contact number

Figure 15. Contact fabric at shaft mid-height projected on the *c-z*, *r-z*, and *c-r* plane: (a) total contact force and (b) contact number.

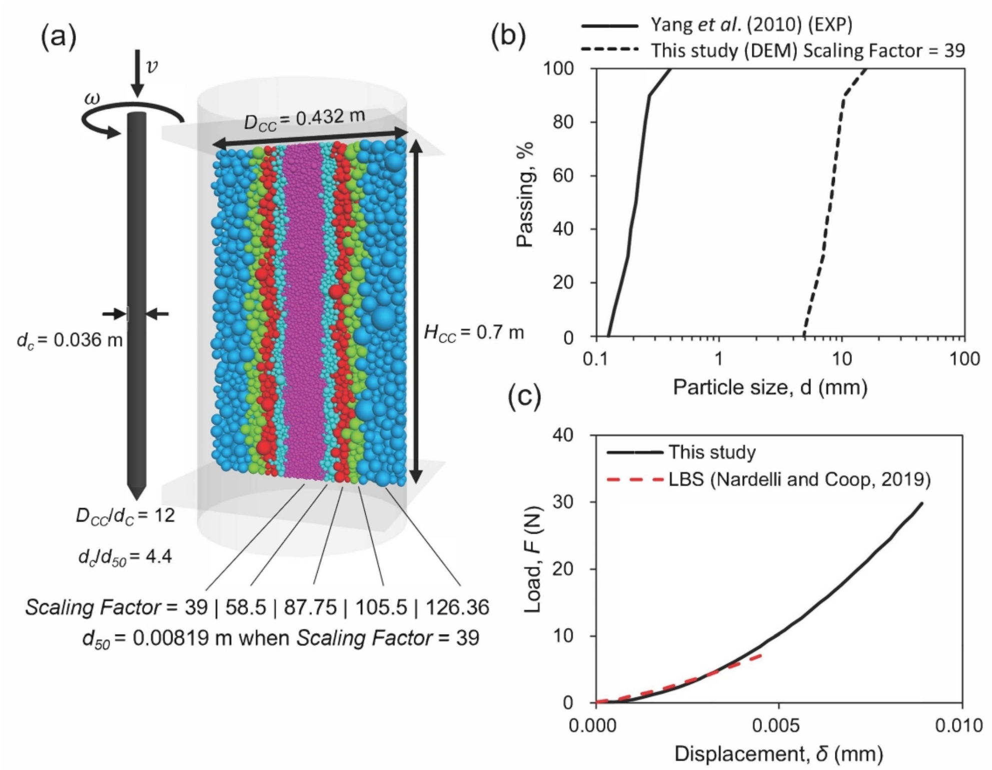

Figure 1. (a) Layout of chamber and probe, (b) particle size distribution of Fontainebleau sand, and (c) reproduction of the load-displacement curve from a single grain test.

567x436mm (163 x 163 DPI)

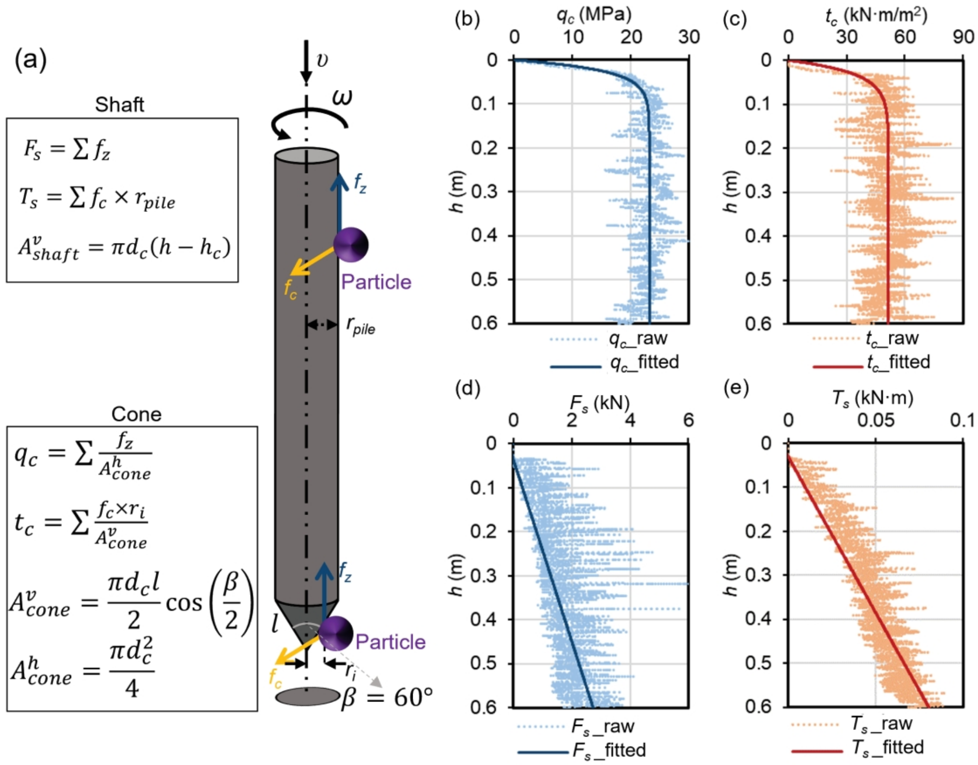

Figure 2. (a) Schematic illustration of force calculations and soil resistances on the cone and shaft of rotary CPT with *SR* = 2: (b) tip resistance q_c, (c) torque on the cone t_c, (d) vertical friction force on the whole shaft F_s and (e) torque on the whole shaft T_s vs depth.

627x487mm (600 x 600 DPI)

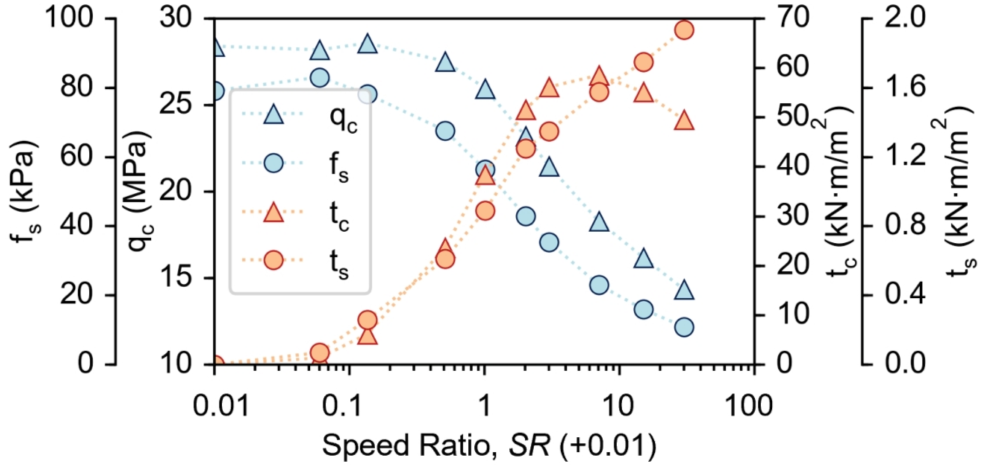

Figure 3. Rotation effects on the fitted value of tip resistance q_c, vertical friction force on the shaft f_s, torque on the cone t_c, and torque on the shaft t_s.

392x190mm (300 x 300 DPI)

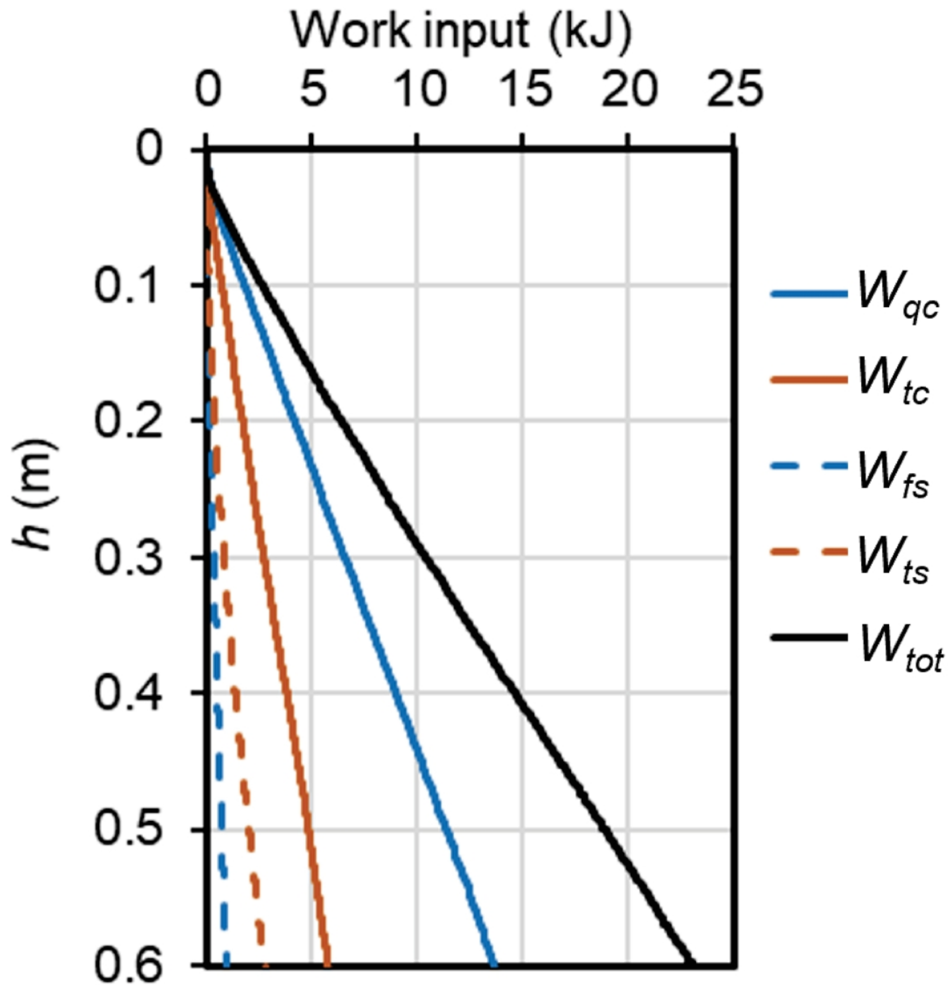

Figure 4. Work done at the cone and shaft during the rotary penetration for the case of *SR*=2.

237x239mm (300 x 300 DPI)

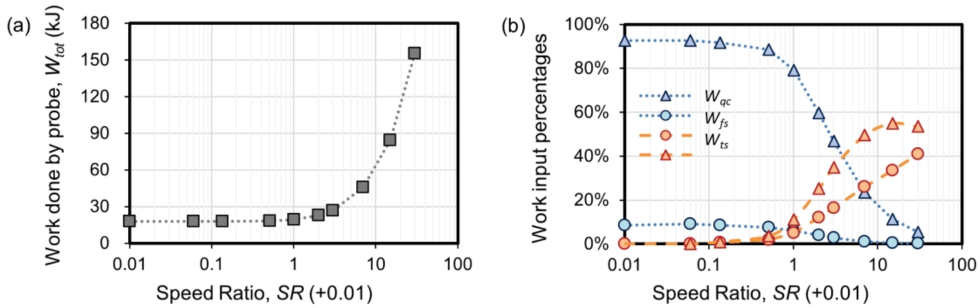

Figure 5. Effect of rotation on (a) total work input, and (b) work components on the cone and shaft.

613x190mm (300 x 300 DPI)

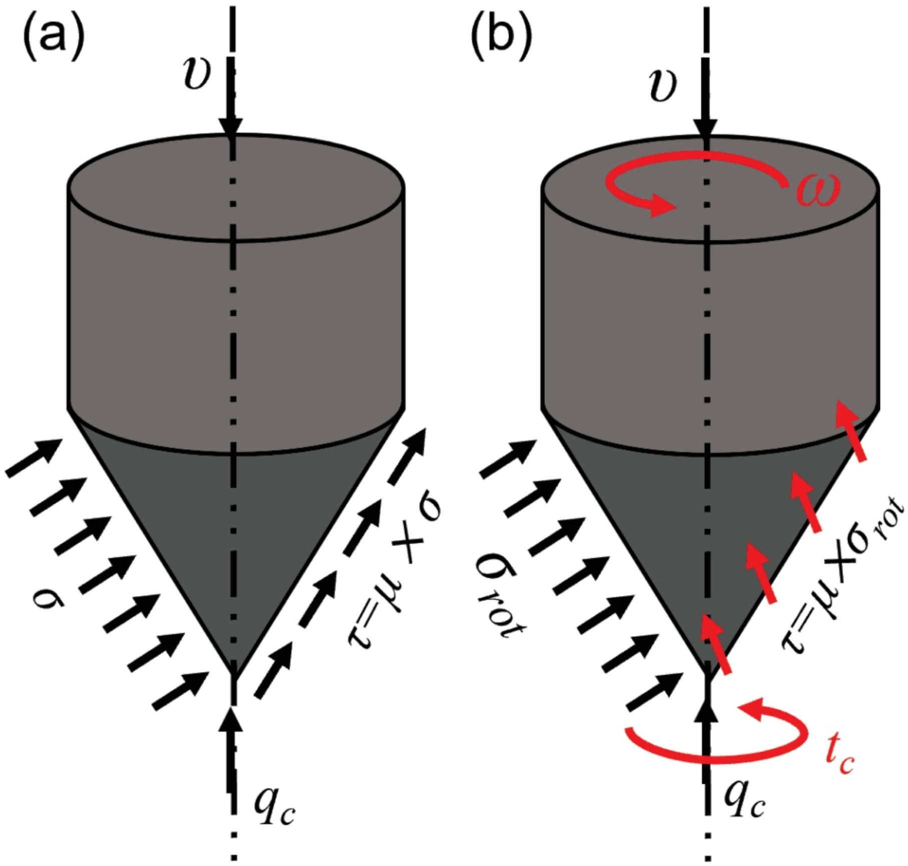

Figure 6. Force diagrams of (a) conventional and (b) rotary penetration test.

317x284mm (300 x 300 DPI)

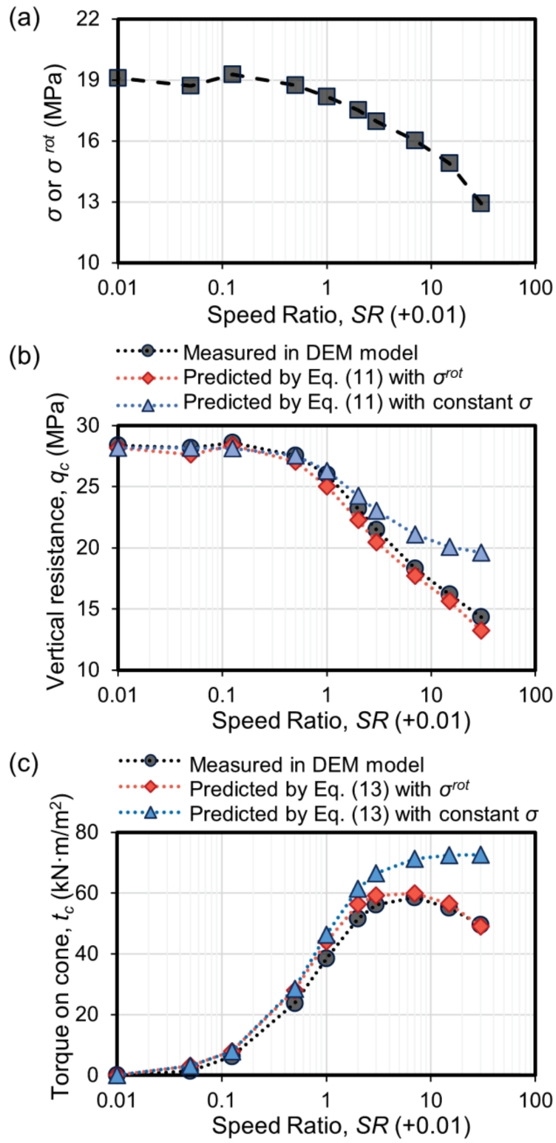

Figure 7. (a) Measured normal stress on the cone, (b) measured and predicted q_c (c) measured and predicted t_c versus SR+0.01.

295x615mm (600 x 600 DPI)

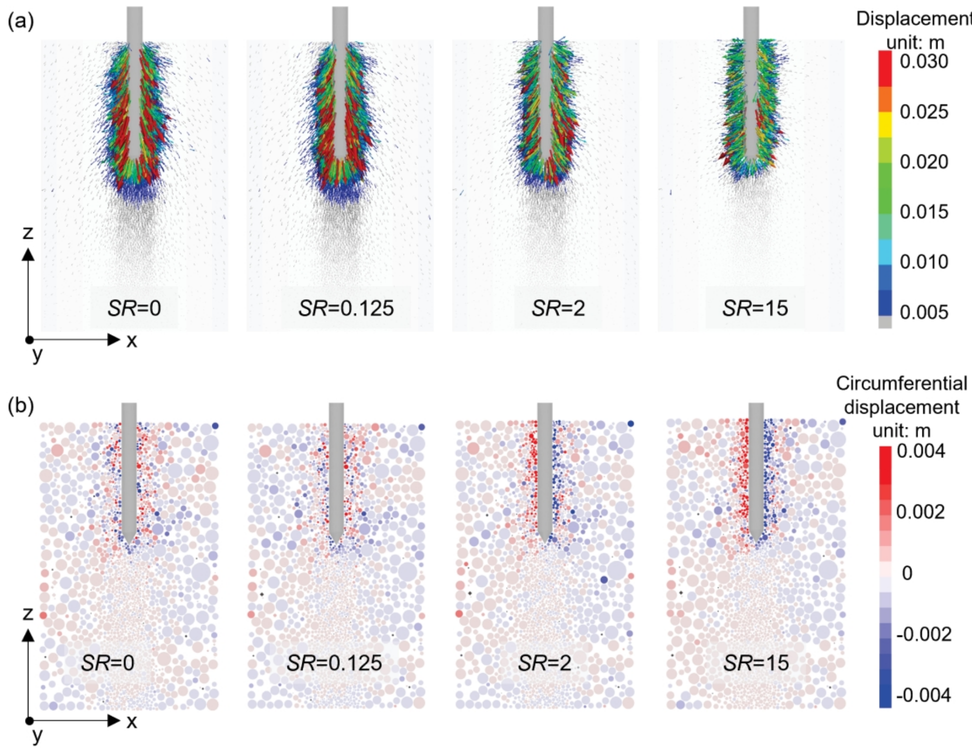

Figure 8. (a) Particle displacement vectors projected on central vertical plane of a vertical section with the thickness of d_c, and (b) circumferential component of the displacement vectors in (a) when the probe penetrates to the depth of 0.3m.

556x422mm (600 x 600 DPI)

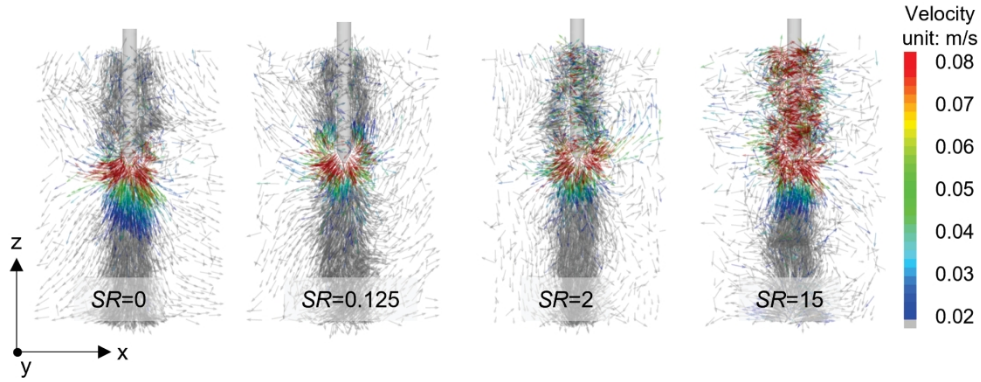

Figure 9. Particle velocity field projected on central vertical plane of a vertical section with the thickness of d_c when the probe penetrates to the depth of 0.3m.

543x216mm (600 x 600 DPI)

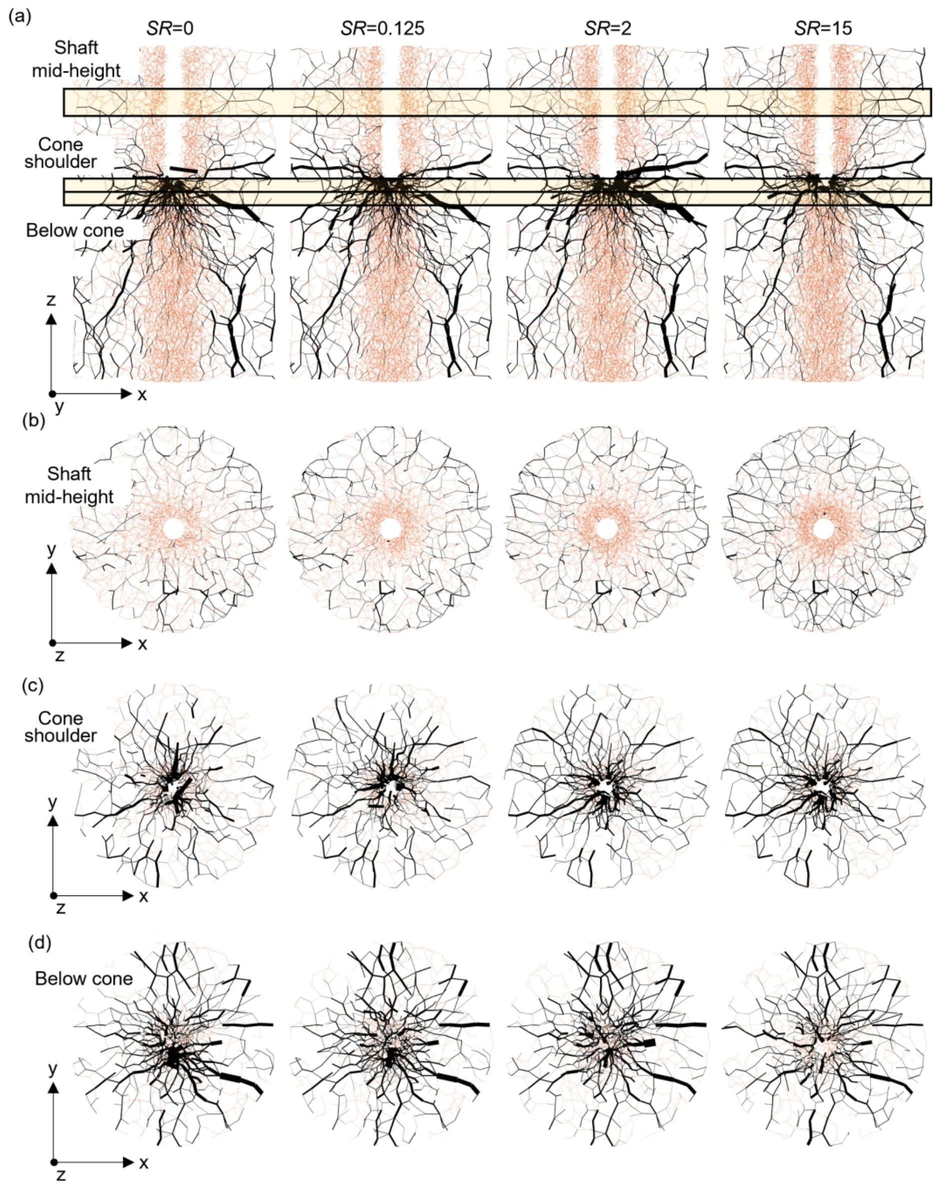

Figure 10. Contact force network of a vertical slice with the thickness of d_c (a) projected on the central vertical plane, and a horizontal slice (b) at shaft mid-height, (c) at cone shoulder, and (d) below cone projected on a horizontal plane when the probe penetrates to the depth of 0.3 m.

595x761mm (600 x 600 DPI)

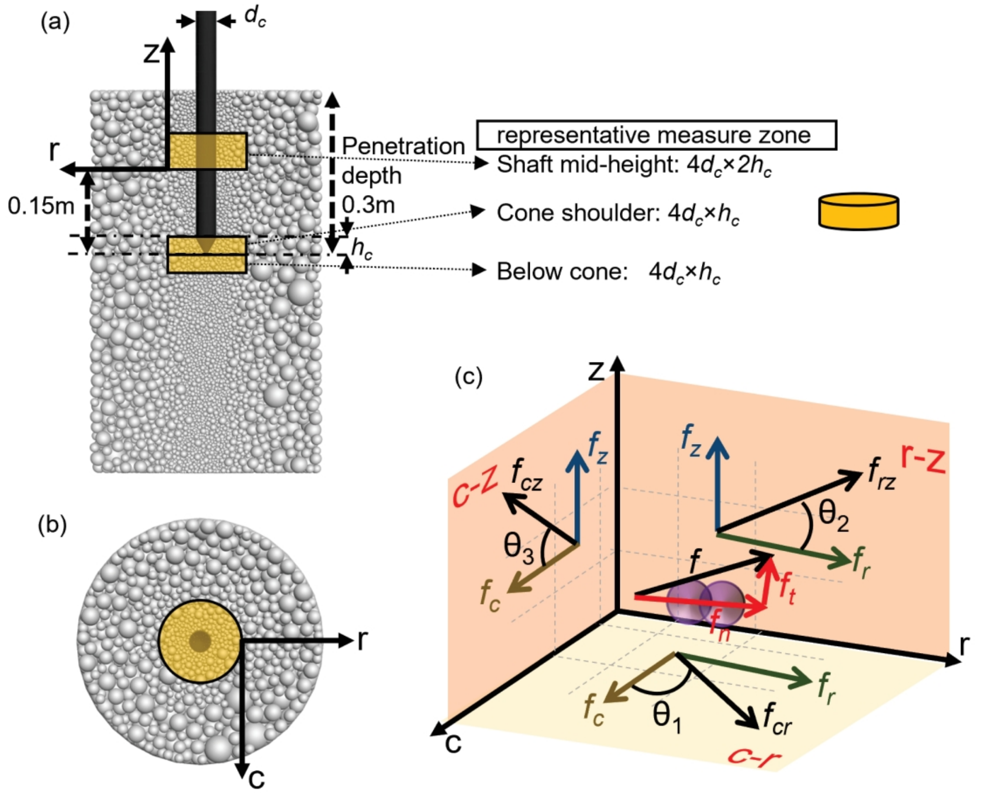

Figure 11. Selection of three representative zones around the probe for microscale characterizations: (a) side view and (b) plan view; (c) example of decomposition of a 3D contact vector in the *z*-*c*-*r* cylindrical coordinate space.

496x411mm (600 x 600 DPI)

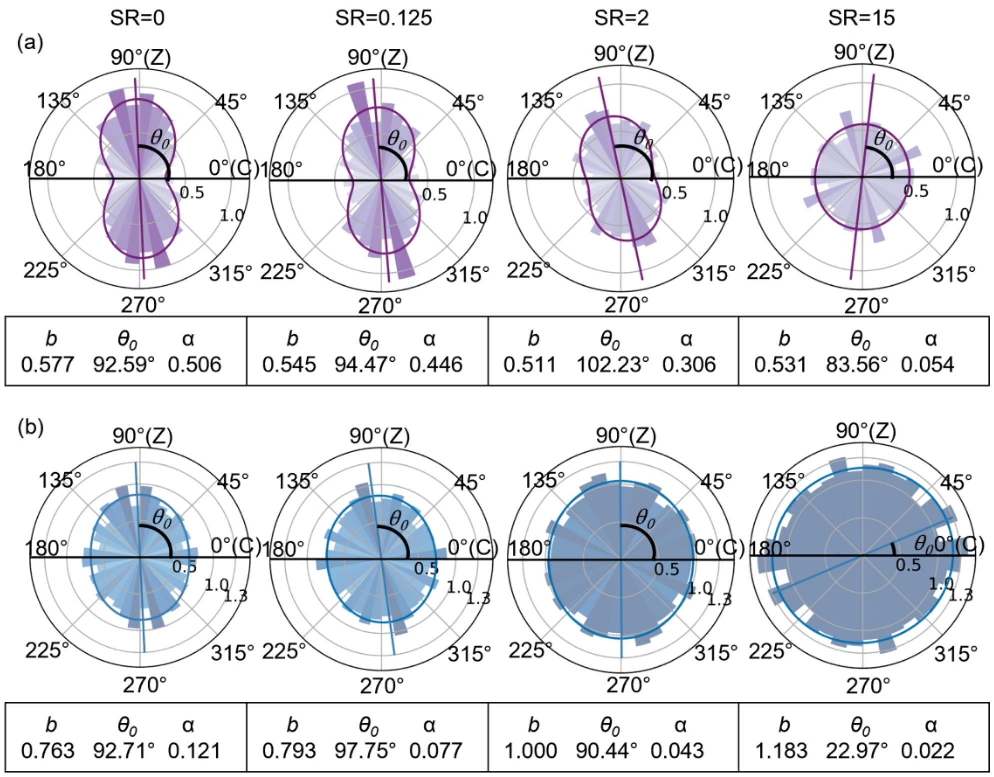

Figure 12. Contact fabric analysis in polar coordinates for the *c-z* projection of the contacts in the cylindrical zone of shaft mid-height: (a) total contact force and (b) contact number.

555x433mm (600 x 600 DPI)

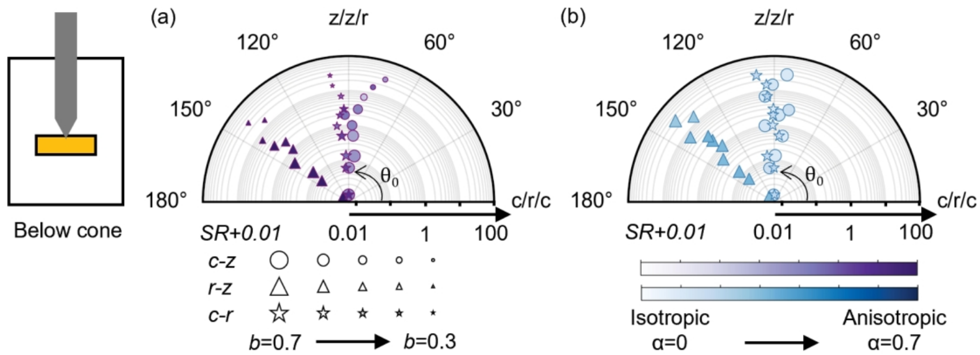

Figure 13. Contact fabric below cone projected on the *c-z*, *r-z*, and *c-r* plane: (a) total contact force and (b) contact number.

464x173mm (300 x 300 DPI)

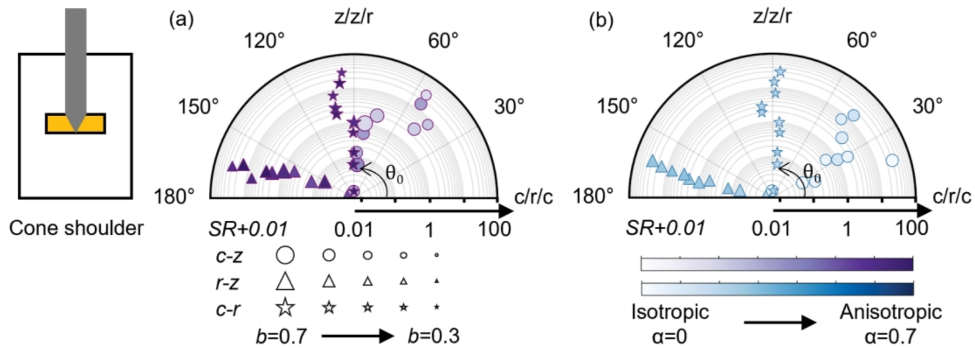

Figure 14. Contact fabric at cone shoulder projected on the *c-z*, *r-z*, and *c-r* plane: (a) total contact force and (b) contact number

471x171mm (300 x 300 DPI)

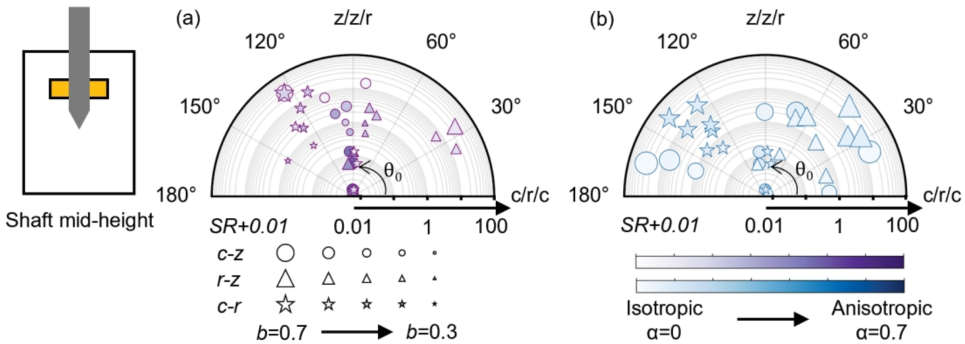

Figure 15. Contact fabric at shaft mid-height projected on the *c-z*, *r-z*, and *c-r* plane: (a) total contact force and (b) contact number.

478x172mm (300 x 300 DPI)